The Astrophysical Journal, 986:32 (10pp), 2025 June 10 https://doi.org/10.3847/1538-4357/add0ac

Polarization Evolution of Gamma-Ray Burst Prompt Emission with Bulk Acceleration

Qian Zhong[1], Hong-Bang Liu[1], Kangfa Cheng[2], Zu-Ke Feng[1], Jiang-Chuan Tuo[1], Qian-Nan Mai[1], Jirong Mao[3,4,5], and En-Wei Liang[1]
[1] Guangxi Key Laboratory for Relativistic Astrophysics, School of Physical Science and Technology, Guangxi University, Nanning 530004, People's Republic of China; liuhb@gxu.edu.cn
[2] School of Mathematics and Physics, Guangxi Minzu University, Nanning 530006, People's Republic of China
[3] Yunnan Observatories, Chinese Academy of Sciences, Kunming 650011, Yunnan Province, People's Republic of China
[4] Center for Astronomical Mega-Science, Chinese Academy of Sciences, 20A Datun Road, Chaoyang District, Beijing 100012, People's Republic of China
[5] Key Laboratory for the Structure and Evolution of Celestial Objects, Chinese Academy of Sciences, Kunming 650011, People's Republic of China
Received 2024 December 17; revised 2025 March 25; accepted 2025 April 23; published 2025 June 4

Abstract

During the prompt phase, Poynting-flux-dominated jets undergo acceleration accompanied by magnetic dissipation. By using an outward-propagating thin-shell model, where bulk Lorentz factors Γ increase with radius and the magnetic field strength decay is related to the acceleration and the energy conversion rate, this process can be investigated through time-resolved polarization analysis. Faster acceleration produces a greater flux, steeper light-curve growth followed by a sharper decline, and polarization degree decreases sharply. With a fixed acceleration index, lower energy conversion rates are associated with lower flux, shallower rises and declines in light curves, lower polarization degree, smoother decline for on-beam ($q = \theta_v/\theta_j < 1$) emission, and sharper decline for off-beam ($q > 1$) emission in polarization curves. Both jet acceleration and magnetic dissipation enhance the likelihood of polarization angle flips in observations with small viewing angles, while also leading to higher polarization degrees after the flip in observations with larger viewing angles. The joint analysis of light curves and polarization provides valuable insights into gamma-ray burst motion and energy conversion processes. Rapid decline in the light curve indicates fast acceleration and high energy conversion rates, while gradual light-curve decline coupled with polarization angle flips (for small viewing angles) or the higher polarization degree after flipping (for large viewing angles) suggests acceleration accompanied by magnetic dissipation. Otherwise, the jet is coasting or slowly accelerating at this time.

Unified Astronomy Thesaurus concepts: Gamma-ray bursts (629); Magnetic fields (994)

1. Introduction

The composition of the gamma-ray burst (GRB) ejecta is commonly characterized by the magnetization parameter $\sigma = F_p/F_b$, where F_p is the Poynting flux and F_b represents the matter flux (B. Zhang & H. Yan 2011). When the magnetization parameter σ is much less than 1, the jet is considered to be dominated by matter flux; otherwise, it is considered as a Poynting-flux-dominated jet.

In the case of matter-dominated jets, the internal shock model is commonly used. The central engine emits multiple shells with varying Lorentz factors, which collide and release energy as the faster shell catches up with the slower one (M. J. Rees & P. Meszaros 1994; M.-X. Lan et al. 2021). For matter-dominated jets, they reach the maximum bulk Lorentz factor and enter the coasting phase before the collision (P. Meszaros & M. J. Rees 1993; H. Gao & B. Zhang 2015). Subsequently, the jet interacts with the external medium and decelerates (G. Ryan et al. 2020).

Poynting-flux-dominated jets are primarily powered by magnetic reconnection (C. Thompson 1994; A. Lazar et al. 2009; B. Zhang & H. Yan 2011; J. C. McKinney & D. A. Uzdensky 2012). A part of the magnetic energy is converted into kinetic energy to accelerate the jet (N. Vlahakis & A. Königl 2003). Jets initially undergo a rapid acceleration phase, followed by a slow acceleration phase. There are two possible scenarios: the jet may enter the coasting phase and then decelerate ($r_s < r_d$), or it may decelerate before reaching the maximum Lorentz factor ($r_s > r_d$). Here, r_s represents the saturation radius, where the jet is dominated by the matter flux ($\sigma_s \ll 1$) and the bulk Lorentz factor remains constant, while r_d is the deceleration radius. Regarding the acceleration of the jet and magnetic field, various conclusions have been given in different papers. Magnetic reconnection is prone to occur when the neighboring magnetic field lines are not parallel (E. N. Parker 1957; A. Lazarian & E. T. Vishniac 1999; P. Kumar & B. Zhang 2015). In G. Drenkhahn (2002) and G. Drenkhahn & H. C. Spruit (2002), the acceleration index is $1/3$ ($\Gamma \propto R^{1/3}$) when polarity field lines reverse, whereas it is less than $1/3$ in the case of other magnetic field configurations. J. Granot et al. (2011) do not require opposite polarity magnetic field lines, still deriving $\Gamma \propto R^{1/3}$. Additionally, the ICMART model, in which shells collide with each other, results in distorted magnetic field lines and triggers magnetic reconnection, which subsequently causes a reconnection-turbulence avalanche that releases magnetic field energy and accelerates the jet dramatically (B. Zhang & H. Yan 2011; H. Gao & B. Zhang 2015). Z. L. Uhm & B. Zhang (2015) investigated the high-latitude emission for jets undergoing bulk acceleration and deceleration. In a subsequent study, Z. L. Uhm & B. Zhang (2016a) investigated X-ray flares undergoing rapid acceleration, with an acceleration index much larger than $1/3$. The prompt emission may also experience rapid acceleration due to the similar origin to X-ray flares (Z. L. Uhm & B. Zhang 2016b). Z. L. Uhm &

B. Zhang (2016b) studied the spectral lags in prompt emission and concluded that their production requires rapid bulk acceleration.

Polarization serves as a valuable probe for GRBs. For instance, polarization can reveal the jet structure, including top-hat jets ("homogeneous" jets) and structured jets (E. M. Rossi et al. 2004; R. Gill & J. Granot 2021). It can also study the radiation mechanisms (K. Toma et al. 2009), magnetic field configurations (M.-X. Lan et al. 2016; R. Gill & J. Granot 2021), and magnetic field structure evolution (J.-C. Tuo et al. 2024). The polarization of the prompt emission of GRBs has been studied. R. Gill & J. Granot (2021) studied polarization of kinetic-energy-dominated flow and Poynting-flux-dominated flow, introducing slow acceleration, but not taking into account the rapid acceleration and extra decay of the magnetic field strength. K. F. Cheng et al. (2020) have discussed polarization properties under decaying magnetic fields, but do not discuss the situation when bulk acceleration occurs. M.-X. Lan & Z.-G. Dai (2020) considered acceleration and decaying magnetic fields. However, faster acceleration and the combination of both were not considered. Therefore, this part will be further explored in this paper.

POLAR was launched in 2016 and obtained 14 GRB results (M. Kole et al. 2020). LEAP, SPHiNX, and POLAR-2 will also be launched in the near future (M. Kole 2019; M. Pearce et al. 2019; R. Gill et al. 2021; C. A. Wilson-Hodge et al. 2021; Z.-K. Feng et al. 2024). Polarization observation will play a more and more important role in GRB research as another perspective, and thus the study of polarization is essential.

In this paper, we will present the following. In Section 2, a brief description of the models and the methodology used to calculate the polarization evolution are provided. The effects on polarization when bulk acceleration and magnetic dissipation occur will be described in Section 3. Finally, we will discuss and conclude the results in Section 4 and Section 5, respectively.

2. Models and Method

2.1. Models

Z. L. Uhm & B. Zhang (2016b) introduced a model involving an ultrarelativistic thin shell to study GRB prompt emission, which was further improved in Z. L. Uhm et al. (2018). In this paper, the same model as in Z. L. Uhm et al. (2018) is adopted, except for the definition of the coefficient b, which will be detailed later. The model describes a radial expansion of a shell that begins emission at turn-on radius $r_{\rm on}$, and at a radius $r_{\rm off}$ the emission is turned off, beyond which the emission is from the high-latitude region. The lab-frame times at which the GRB emission turns on and off are $t_{\rm on}$ and $t_{\rm off}$, respectively. At the onset of expansion, the shell contains no electrons ($N = 0$ at $r_{\rm on}$), but as the shell expands, electrons are injected at a constant rate $R'_{\rm inj}$. The total number of electrons in the shell at a comoving time t' is denoted as $N(t')$, where the prime indicates quantities measured in the comoving frame. In this model, the bulk Lorentz factor Γ and the characteristic electron Lorentz factor $\gamma_{\rm ch}$ all vary with radius, i.e.,

$$\Gamma(r) = \Gamma_0 \left(\frac{r}{r_{\rm on}}\right)^s, \tag{1}$$

$$\gamma_{\rm ch}(r) = \gamma^0_{\rm ch} \left(\frac{r}{r_{\rm on}}\right)^g, \tag{2}$$

where Γ_0 and $\gamma^0_{\rm ch}$ represent the values of Γ and $\gamma_{\rm ch}$ at the radius $r_{\rm on}$, respectively.

According to the magnetic flux conservation, the poloidal magnetic field component decreases with radius: $B'_r \propto r^{-2}$, and the toroidal component decreases as $B'_{\theta\phi} \propto r^{-1}$ when there is no significant dissipation of magnetic energy (Z. L. Uhm & B. Zhang 2014; R. Gill & J. Granot 2021). Since GRB prompt emission occurs at a large radius, the toroidal component magnetic field dominates with $B' \propto r^{-1}$. However, when the magnetic energy is converted to other types of energy and magnetic dissipation occurs, there should be an additional decay in the magnetic field strength. We introduce a coefficient b that describes the additional decay, which is related to the rate of converting magnetic energy into kinetic energy. The evolution of the magnetic field strength in the comoving frame B' can then be expressed as

$$B'(r) = B'_0 \left(\frac{r}{r_{\rm on}}\right)^{-(1+b\cdot s)}, \tag{3}$$

where B'_0 represents the values of B' at $r_{\rm on}$ and s is the acceleration index.

2.2. Methods

Photons emitted from different latitudes at the same time will reach the observer at different times. In other words, photons observed at the same observer time are actually emitted at different times, radii, and latitudes. This phenomenon is referred to as the equal-arrival time surface (EATS; R. Sari 1998). The observer time $t_{\rm obs}$ at which a photon emitted from a radius r and latitude θ at time t reaches the observer is given by (Z. L. Uhm & B. Zhang 2016b)

$$t_{\rm obs} = \left[\left(t - \frac{r}{c}\cos\theta\right) - \left(t_{\rm on} - \frac{r_{\rm on}}{c}\right)\right](1+z), \tag{4}$$

where θ is the angle between the velocity of the jet element and the observer's line of sight (LOS), c is the speed of light, and z is the redshift. The time t at which a photon is emitted from a radius r can be calculated by $t = \int_{r_{\rm on}}^{r} \frac{dr}{v} + t_{\rm on}$, where $v = \beta c$ and $\beta = \sqrt{1 - \frac{1}{\Gamma^2}}$.

In this paper, we use the empirical Band function to describe the photon spectrum of electrons, as it well fits the observed photon spectrum in GRB prompt emission. The Band function consists of two smoothly connected power laws, where low- and high-energy photon spectral indices are α_B and β_B, respectively. It is defined as (D. Band et al. 1993)

$$H(x) = \begin{cases} x^{\alpha_B+1}\exp(-x), & \text{if } x \leqslant x_c, \\ x_c^{x_c}\exp(-x_c)x^{\beta_B+1}, & \text{if } x > x_c, \end{cases} \tag{5}$$

where $x = \nu'/\nu'_{\rm ch}$, $x_c \equiv \alpha_B - \beta_B$.

The single electron spectral power and the characteristic frequency of the electron $\nu'_{\rm ch}$ as derived by G. B. Rybicki & A. P. Lightman (1979) are given by

$$P_0 = \frac{3\sqrt{3}\, m_e c^2 \sigma_T B'}{32 q_e}, \tag{6}$$

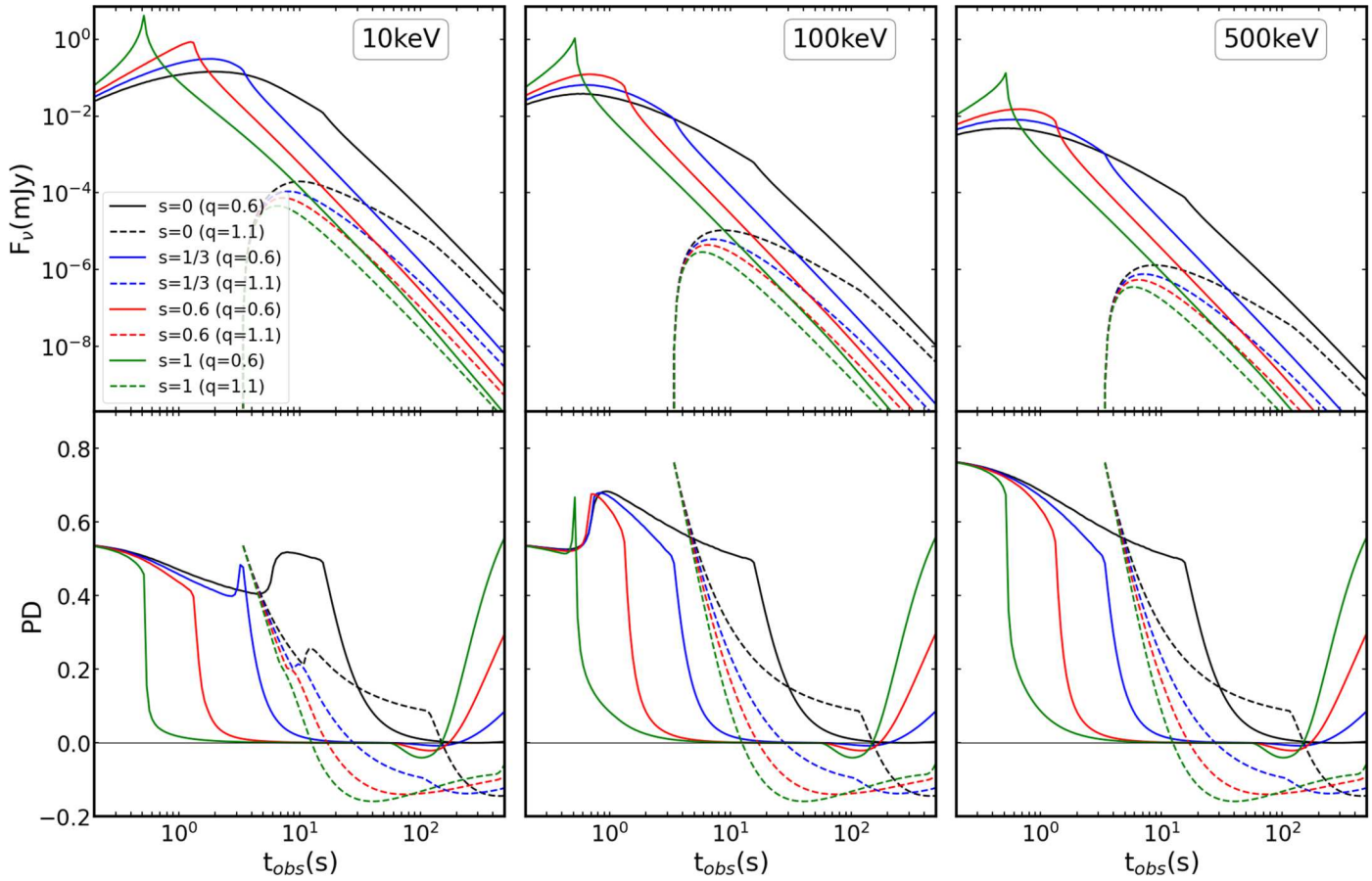

Figure 1. Light curves and polarization evolution with large-scale ordered toroidal magnetic field. Black blue, red, and green represent models [1a] ($s = 0$), [2a] ($s = 1/3$), [3a] ($s = 0.6$), and [4a] ($s = 1$), respectively. The solid line indicates on-beam emission ($q = 0.6$), while the dashed line indicates off-beam emission ($q = 1.1$). The top row shows the light curves, and the bottom row shows the polarization curves. The left, middle, and right columns correspond to $h\nu = 10$, 100, and 500 keV, respectively.

$$\nu'_{\rm ch} = \frac{q_e B' \sin\theta'_B \gamma^2_{\rm ch}}{2\pi m_e c}, \tag{7}$$

where σ_T is the Thomson cross section. m_e and q_e are the electron mass and charge, respectively. The pitch angle of electrons θ'_B is defined as (K. Toma et al. 2009; M.-X. Lan et al. 2016)

$$\sin\theta'_B = \left[1 - D^2 \frac{\sin^2\theta\cos^2\varphi}{\cos^2\theta + \sin^2\theta\cos^2\varphi}\right]^{1/2}. \tag{8}$$

Here, φ is defined as the angle in the plane of the sky between the projection of the jet element's velocity and the projection of the magnetic field. The Doppler factor $D = 1/\Gamma(1 - \beta\cos\theta)$. For toroidal magnetic field,

$$\cos\varphi = \frac{\sin\theta_V\cos\theta\sin\phi}{\sqrt{\cos^2\theta_V\sin^2\theta\sin^2\phi + (\sin\theta_V\cos\theta - \cos\theta_V\sin\theta\cos\phi)^2}}, \tag{9}$$

where ϕ is the angle between the projected velocity vector of the jet element and the projected jet axis in the plane of the sky. θ_v is the viewing angle.

The observed spectral flux F_ν and the Stokes parameters Q_ν and U_ν can be obtained by integrating the emission from an EATS as follows (Z. L. Uhm & B. Zhang 2015; J.-J. Geng et al. 2018; M.-X. Lan & Z.-G. Dai 2020):

$$F_\nu = \frac{1+z}{4\pi D_L^2}\int_0^{\theta_+} D^3\sin\theta\, d\theta \int_{-\Delta\phi}^{\Delta\phi} \frac{NP'_0 H(x)\sin\theta'_B}{4\pi}\, d\phi, \tag{10}$$

$$Q_\nu = \frac{1+z}{4\pi D_L^2}\int_0^{\theta_+} D^3\sin\theta\, d\theta \int_{-\Delta\phi}^{\Delta\phi} \times \Pi_p\cos 2\chi_p \frac{NP'_0 H(x)\sin\theta'_B}{4\pi}\, d\phi, \tag{11}$$

$$U_\nu = \frac{1+z}{4\pi D_L^2}\int_0^{\theta_+} D^3\sin\theta\, d\theta \int_{-\Delta\phi}^{\Delta\phi} \times \Pi_p\sin 2\chi_p \frac{NP'_0 H(x)\sin\theta'_B}{4\pi}\, d\phi, \tag{12}$$

where the observed frequency $\nu = \nu' D/(1+z)$, $\theta_- = |\theta_j - \theta_v|$, $\theta_+ = \theta_j + \theta_v$, θ_j is the jet half-opening angle. D_L is the luminosity distance. The limit of integration, $\Delta\phi$, is given by (X. F. Wu et al. 2005) as

$$\Delta\phi = \begin{cases} \pi\Theta(\theta_j - \theta_v), & \theta \leqslant \theta_-, \\ \arccos\left(\frac{\cos\theta_j - \cos\theta_v\cos\theta}{\sin\theta_v\sin\theta}\right), & \theta_- < \theta < \theta_+, \\ 0, & \theta \geqslant \theta_+, \end{cases}$$

where Θ is the Heaviside step function.

The local polarization degree Π_p and local polarization angle χ_p are shown below (K. Toma et al. 2009; M.-X. Lan

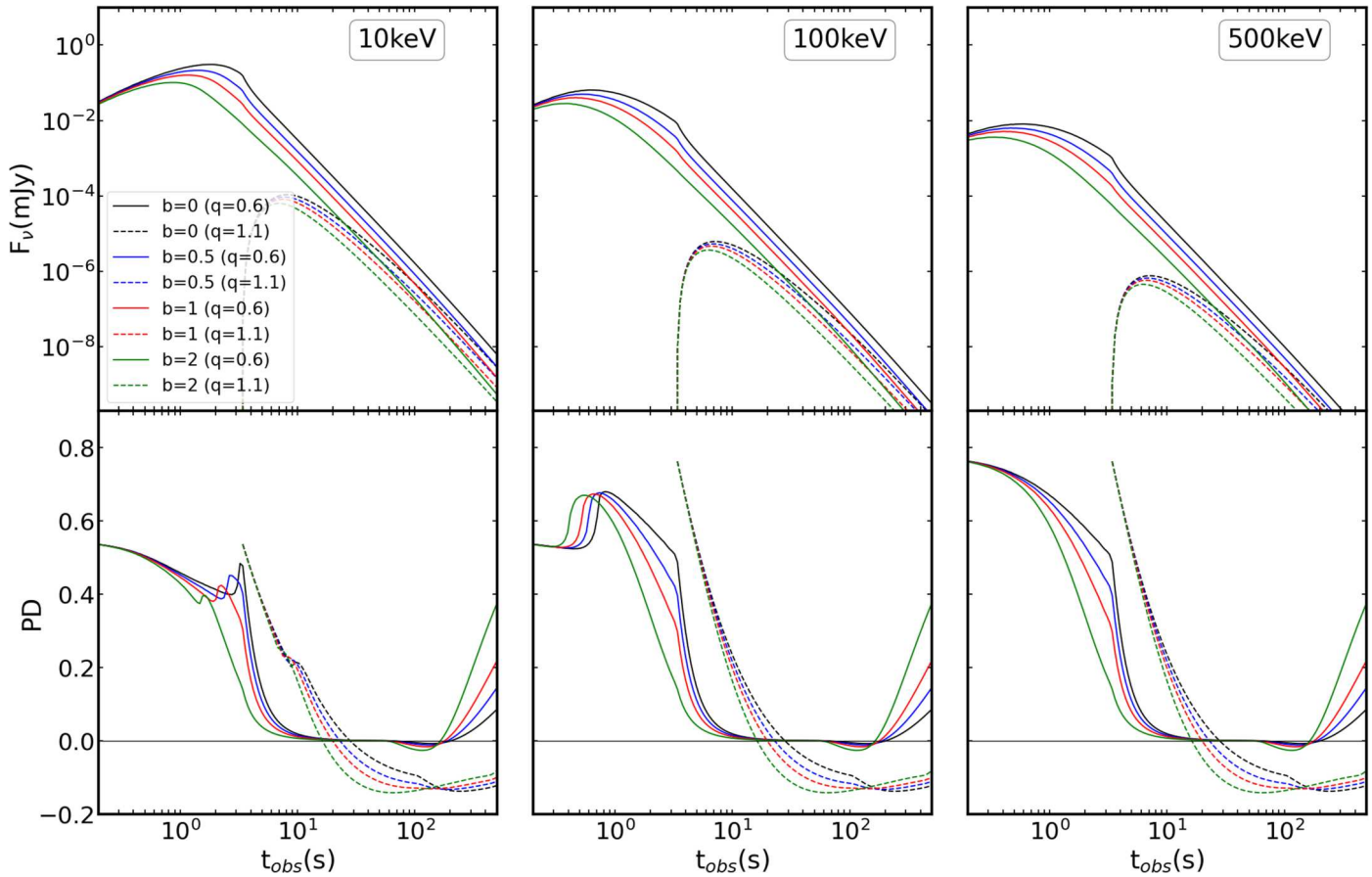

Figure 2. Light curves and polarization evolution with large-scale ordered toroidal magnetic field. Black, blue, red, and green represent models [2a] ($b = 0$), [2b] ($b = 0.5$), [2c] ($b = 1$), and [2d] ($b = 2$), respectively. The solid line indicates on-beam emission ($q = 0.6$), while the dashed line represents off-beam emission ($q = 1.1$). The top row shows the light curves, and the bottom row shows the polarization curves. The left, middle, and right columns correspond to $h\nu = 10$, 100, and 500 keV, respectively.

et al. 2016; L.-Q. Sui & M.-X. Lan 2024):

$$\Pi_p = \frac{\hat{a}}{\hat{a} - \frac{2}{3}}, \tag{13}$$

$$\chi_p = \phi + \arctan \times \left(\frac{\cos\theta - \beta}{1 - \beta\cos\theta} \frac{\sin\theta_v \sin\phi}{\cos\theta_v \sin\theta - \sin\theta_v \cos\theta \cos\phi} \right). \tag{14}$$

Here, $\hat{a}$ equals α_B when $x \leqslant x_c$, and $\hat{a} = \beta_B$ when $x > x_c$.

When the magnetic field is toroidal and axisymmetric with respect to the jet axis, the Stokes parameter U_ν is equal to zero due to symmetry. Therefore, the polarization degree Π can be expressed as

$$\Pi = \frac{Q_\nu}{F_\nu}. \tag{15}$$

The sign of the polarization degree indicates the direction of polarization. A change in the sign of Π from positive to negative (or vice versa) implies that the polarization angle has rotated by 90°.

3. Numerical Results

3.1. Bulk Acceleration

This section explores the effect of bulk acceleration on the evolution of polarization. All of the models in this section assume no additional decay of the magnetic field, i.e., $B' \propto r^{-1}$ ($b = 0$). The cases where magnetic energy dissipation plays an essential role will be discussed in Section 3.2.

The initial magnetic field strength $B_0 = 30$ G and bulk Lorentz factor $\Gamma_0 = 250$. For the acceleration indices s in Equation (1), several values between 0 (coasting) and 1 (fast acceleration) were chosen: 0, 1/3, 0.6, and 1, for models [1a], [2a], [3a], and [4a], respectively. Since the polarization properties of the toroidal magnetic field approximate those of the aligned magnetic field when the viewing angle is nonzero (M.-X. Lan & Z.-G. Dai 2020), we adopt the toroidal magnetic field here. The models are calculated for both on-beam ($q = \theta_v/\theta_j = 0.6$) and off-beam ($q = 1.1$) emissions, where the jet half-opening angle is $\theta_j = 0.1$ rad. The other parameters of our models are consistent with the "i" models in Z. L. Uhm et al. (2018), with the following values: $\alpha_B = -0.8$, $\beta_B = -2.3$, $R'_{\rm inj} = 10^{47}$ s^{-1}, $\gamma^0_{\rm ch} = 5 \times 10^4$, $g = -0.2$, $r_{\rm on} = 10^{15}$ cm, and $r_{\rm off} = 3 \times 10^{16}$ cm. The initial radius is chosen to be 10^{15} cm, which is the typical emission radius for the ICMART model (H. Gao & B. Zhang 2015). The redshift is set to $z = 1$, and the standard flat ΛCDM universe model is applied with the following parameters: $H_0 = 68$ km s^{-1} Mpc^{-1}, $\Omega_m = 0.31$, and $\Omega_\Lambda = 0.69$.

The results are shown in Figure 1. It is clear that the flux of faster-acceleration models is higher than for lower acceleration ones. Additionally, light curves associated with constant Γ exhibit mild rises and gradual declines, whereas those

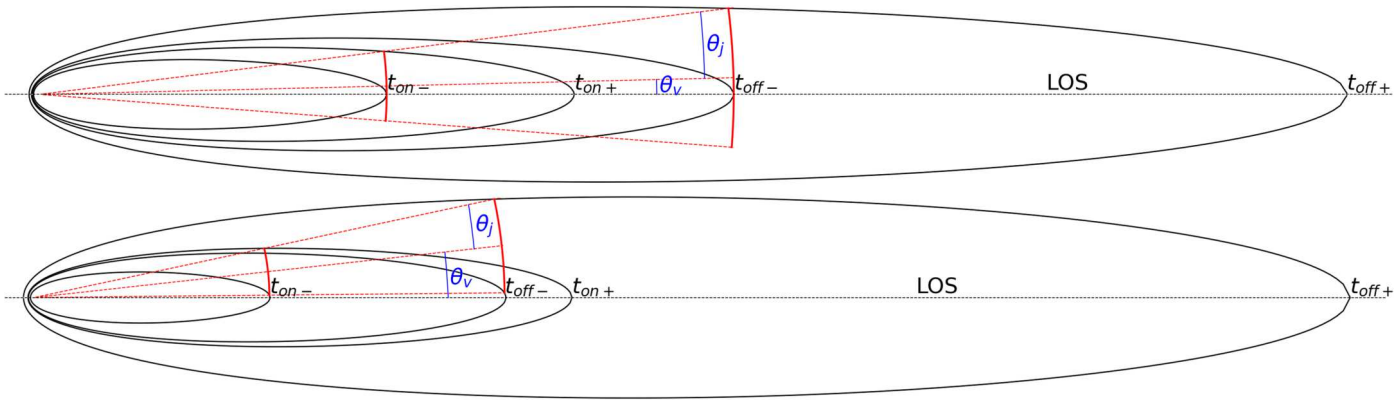

Figure 3. Schematic of EATSs in a 2D plane, where the jet undergoes acceleration, i.e., $s > 0$. The black solid lines represent EATSs, the red solid line is the range of the jet, and the red dashed line is the jet edges and the symmetry axis. The upper panel shows the on-beam emission ($q < 1$), and the lower panel shows the off-beam emission ($q > 1$). $t_{on-} < t_{on+}$, $t_{off-} < t_{off+}$, $t_{on-} < t_{off-}$, $t_{on+} < t_{off+}$. The sequence of times depends on the magnitude of t_{on+} and t_{off-}. There are two different combinations: $t_{on-} < t_{on+} < t_{off-} < t_{off+}$ and $t_{on-} < t_{off-} < t_{on+} < t_{off+}$.

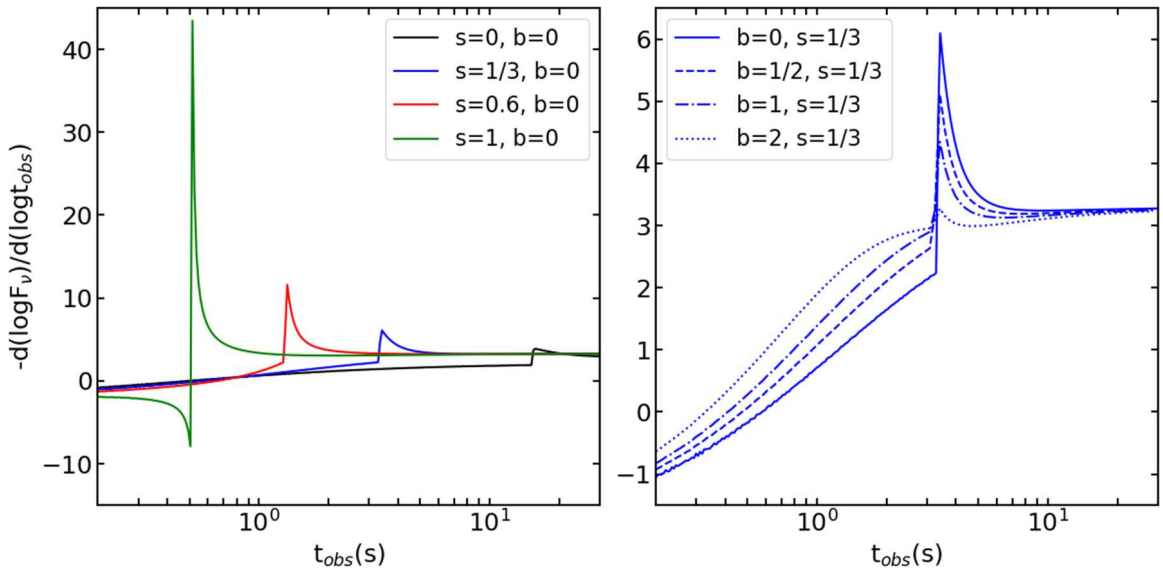

Figure 4. The temporal index $-d(\log F_{\nu_{\rm obs}}^{\rm obs})/d(\log t_{\rm obs})$ of the light curves at 500 keV. These results are calculated from on-beam cases. Black, blue, red, and green represent acceleration indices $s = 0$, $1/3$, 0.6, 1, respectively. The solid, dashed, dashed–dotted, and dotted lines correspond to decay coefficient $b = 0$, $1/2$, 1, 2, respectively. The left panel shows the indices for the "a" models, while the right panel represents the indices for models [2a], [2b], [2c], and [2d].

undergoing acceleration display steep rises followed by sharp declines, which is consistent with Z. L. Uhm & B. Zhang (2015). In the case of rapid acceleration, the decline time coincides with the turn-off time, whereas for slower acceleration or coasting cases, the decline occurs earlier than the turn-off time.

The polarization degree initially matches the local polarization degree and then decreases. The increase in polarization degree is primarily due to the decrease in the electron's characteristic Lorentz factor at larger radius, leading to a higher local polarization degree, and this is why the polarization degree of high energy is higher than that of low energy. In addition, for low-energy emission, it is difficult to see the rise in polarization curves when the jet undergoes fast acceleration. After the emission turned off, the polarization degree dramatically decreases to 0. The larger the acceleration index, the steeper the polarization decay, and the earlier the flip occurs. For small viewing angle case, moving at a constant speed will not exhibits a flip in polarization angle, whereas it flips in acceleration cases. In addition, faster acceleration results in a higher polarization degree after the first flip, which makes it easier to observe. For on-beam cases, a second flip occurs soon after the initial flip. At later times, the polarization degree increases. In models with larger acceleration indices, the polarization degree rises more rapidly.

Table 1
Characteristic Times

Viewing Angle	Acceleration Index (s)	t_{on-} (s)	t_{on+} (s)	t_{off-} (s)	t_{off+} (s)
0.6	0	0	852.10	15.48	25578.60
0.6	1/3	0	852.10	3.37	25566.49
0.6	0.6	0	852.10	1.32	25564.43
0.6	1	0	852.10	0.52	25563.63
1.1	0	3.34	1465.62	115.55	43984.07
1.1	1/3	3.34	1465.62	103.44	43971.96
1.1	0.6	3.34	1465.62	101.38	43969.91
1.1	1	3.34	1465.62	100.58	43969.10

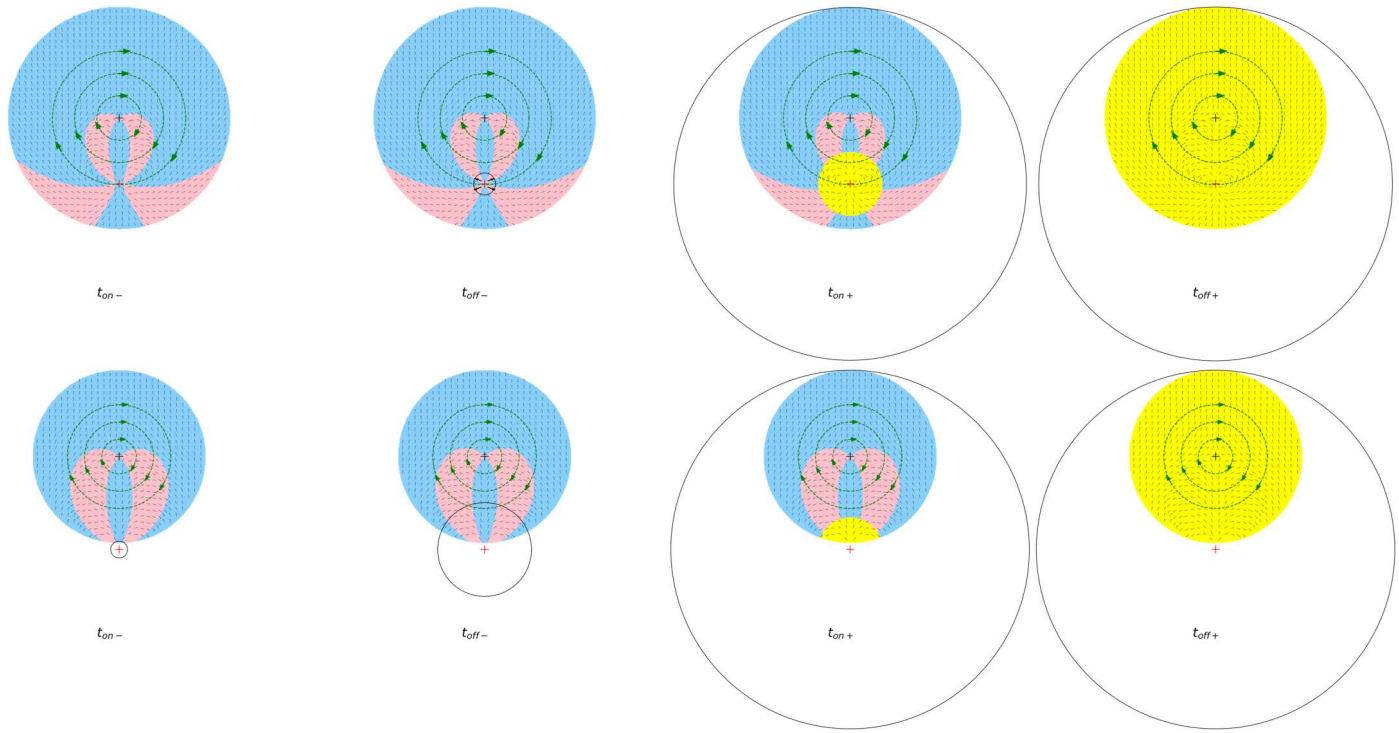

Figure 5. Polarization schematics of a toroidal magnetic field in the plane of the sky for $s = 1/3$. The black plus sign is the jet axis of symmetry, and the red plus sign is the LOS. The black circle is the observed region, and the green dashed line is the direction of the magnetic field. The blue region is polarization along the line connecting the LOS and the jet symmetry axis, while the pink region is transverse to the line. The yellow region is the radiation disappearance after the emission is turned off. The first, second, third, and fourth columns are schematic illustrations of polarization at times t_{on-}, t_{off-}, t_{on+}, and t_{off+}, respectively. The top panels are for on-beam emission and the bottom panels are for off-beam.

3.2. Magnetic Dissipation

The coefficient b in Equation (3) is related to the energy conversion rate. Jets with low energy conversion rates require more magnetic energy to be accelerated, and b is larger. We have calculated the scenarios for $b = 0.5$, 1, and 2 for models [2b], [2c], and [2d], respectively. Models in this section have the same acceleration indies $s = 1/3$ (i.e., [2b]: $B = B_0(r/r_{on})^{-7/6}$, [2c]: $B = B_0(r/r_{on})^{-4/3}$, [2d]: $B = B_0(r/r_{on})^{-5/3}$).

The results are shown in Figure 2. Compared to the model [2a], as the b increases, the light curve decreases earlier, and the rise and decline become slight in general, which is similar to the effects observed in the slower acceleration cases in Section 3.1. Polarization in cases of significant magnetic dissipation exhibits an earlier rise followed by a subsequent fall for on-beam emission. However, the time at which the polarization decreases to zero remains largely unchanged, with the decay occurring at a smooth slope. For off-beam emission, the polarization drops more sharply with larger coefficient b. As the magnetic field strength decays, the polarization degree is higher after polarization angle flipping, and the flip occurs earlier. This trend mirrors the behavior observed in faster-acceleration GRBs discussed in Section 3.1.

4. Discussion

To explain these phenomena, four characteristic observer times related to photon arrival are defined. t_{on-} is the time at which the observer receives the first photon from the emission region, and t_{on+} is the time at which the observer receives the last photon emitted at the turn-on radius. t_{off-} is the time when the observer receives the first photon from the turn-off radius, and t_{off+} is the time at which the observer receives the last photon from the emission, after which the observed flux is zero. Depending on factors such as the bulk Lorentz factor, the viewing angle, the turn-on radius, and the turn-off radius, photons may arrive in different sequences. For instance, the observer may receive photons from the outer edge of r_{on}, followed by photons from the nearer edge at r_{off}. This scenario results in $t_{on+} < t_{off-}$ (shown in the top panel of Figure 3). Alternatively, if the opposite sequence occurs, $t_{on+} > t_{off-}$ (shown in the bottom panel of Figure 3). t_{on-} in the case of on-beam observation is defined as time zero. The characteristic times for each model are summarized in Table 1.

Figure 3 presents a simplified schematic of the 2D cross sections of EATSs for jets under acceleration. The surface shape resembles an egg, with the larger radius side appearing more elongated, in agreement with Z. L. Uhm & B. Zhang (2015). However, when the jet is in constant motion, the EATS forms an elliptical shape (Z. L. Uhm & B. Zhang 2015).

Z. L. Uhm & B. Zhang (2015) also calculated the temporal indices $-d(\log F_{\nu_{obs}}^{obs})/d(\log t_{obs})$ of light curves. The indices of our models are shown in Figure 4. Faster acceleration without magnetic dissipation results in a sharper rise and a steeper decline in the light curve, consistent with Z. L. Uhm & B. Zhang (2015). However, for slower acceleration models, our models exhibit a decline prior to the turn-off time, which differs from Z. L. Uhm & B. Zhang (2015), as they assume a constant magnetic field. In contrast, acceleration jets with more significant magnetic dissipation display a shallower increase and decrease in their light curves, closely resembling the evolution patterns observed in cases of slower acceleration without magnetic dissipation. This similarity makes it challenging to distinguish between scenarios of slow acceleration with negligible magnetic dissipation and fast

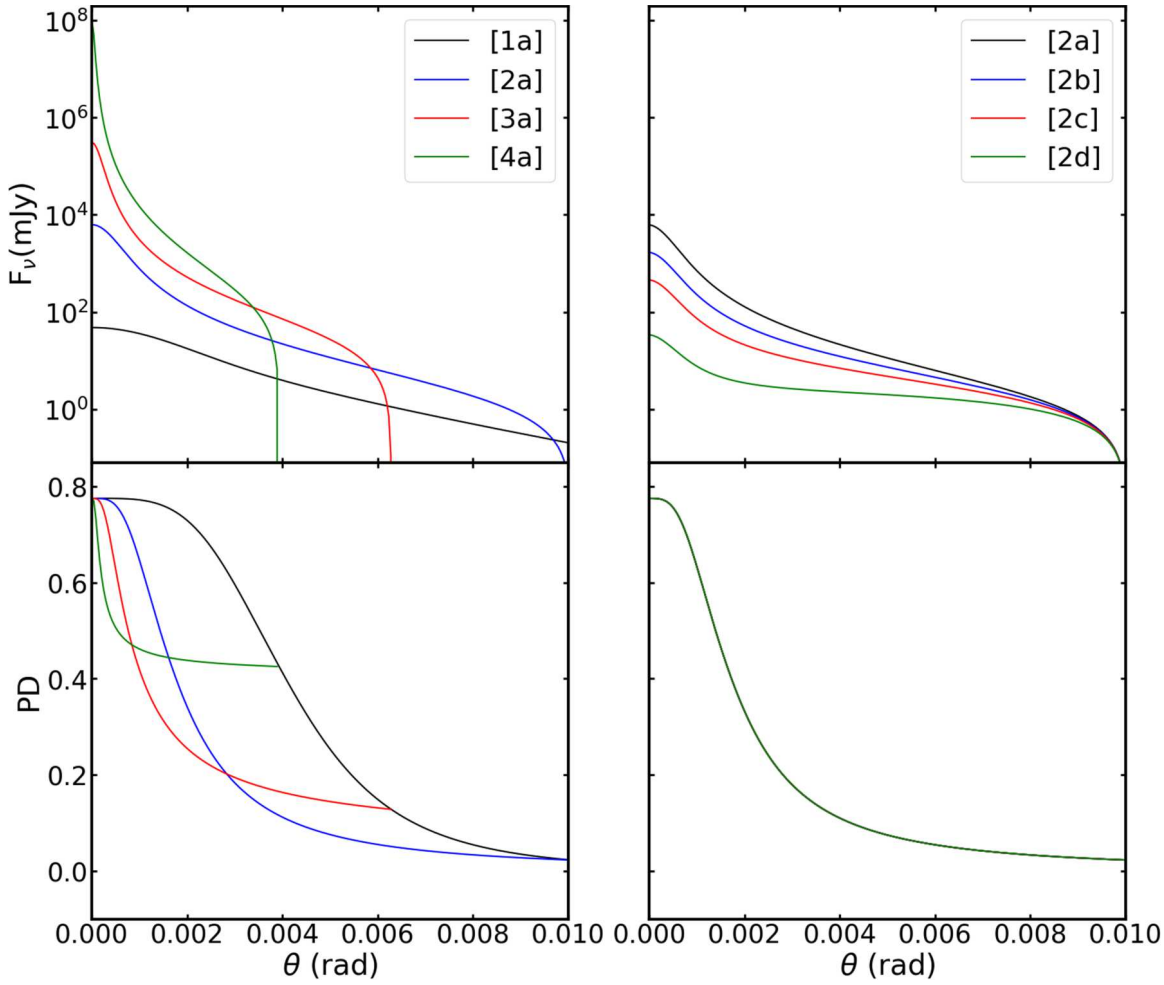

Figure 6. Distribution of local flux and polarization degree with θ, $h\nu = 500$ keV, $t = t_{\rm off-}$. Top panels show the distribution of flux, and bottom panels show the PD(θ). Purely accelerated models are shown in the left panels, and acceleration with magnetic dissipation models are shown in the right panels.

acceleration with substantial magnetic dissipation solely based on light-curve analysis. However, combining light curves and polarization curves can distinguish between these two scenarios. While slow acceleration without magnetic dissipation generally lacks a pronounced polarization angle flip or shows a low polarization degree after flipping, fast acceleration with magnetic dissipation can exhibit such a flip and a higher polarization degree after the flip, providing a critical observational marker for differentiating these scenarios.

The polarization schematics are shown in Figure 5. Initially, the observation area is narrow, and the field of view is primarily dominated by the blue region both for on-beam and off-beam emission, where the polarization direction on the sky plane aligns to the line that connects the LOS and the jet symmetry axis. Over time, other polarization directions enter the field of view, resulting in a decrease in the overall polarization degree. Subsequently, polarization perpendicular to this line becomes dominant, leading to a flip in the polarization angle. Eventually, the polarization returns to the initial blue region, once again becoming the dominant direction. On-beam emission leads to a second time flip sooner after the first flip compared to the off-beam emission. In addition, the polarization angle evolves over time, particularly in the region close to the LOS. The polarization angle changes over time mainly because of the bulk Lorentz factor evolution. This change causes the polarization degree with high acceleration index to drop more quickly.

To provide more detail than Figure 5, PD(θ) and $f_\nu(\theta)$ are introduced, which denote the local polarization degree and local flux from the θ-circle, respectively (M.-X. Lan & Z.-G. Dai 2020; J.-S. Li et al. 2024). Take $h\nu = 500$ keV as an example.

Figure 6 shows the pattern of PD(θ) and $f_\nu(\theta)$ at $t_{\rm off-}$. As can be seen in the left panels, both the flux and polarization degree of "a" models decrease with increasing θ. Faster acceleration corresponds to a higher local flux at the region close to the LOS, which explains why the observed spectral flux is higher for larger acceleration indices compared to smaller indices. The impact of magnetic field strength decay is illustrated in the right panels of Figure 6. While the magnetic field strength does not affect the local polarization degree, it significantly suppresses the local flux, particularly near the LOS in models [2b], [2c], and [2d] as compared to the [2a] model, leading to a shallower rise and decline in light curves. By reducing local flux, the magnetic field decay effectively diminishes the polarization degree. Consequently, as the decay index of the magnetic field increases, the polarization degree declines earlier and has lower values before the polarization angle flips.

For acceleration jets, the bulk Lorentz factor at the end of emission is significantly larger than the initial value. We compare acceleration models (with $s = 1/3$, 0.6, and 1) to

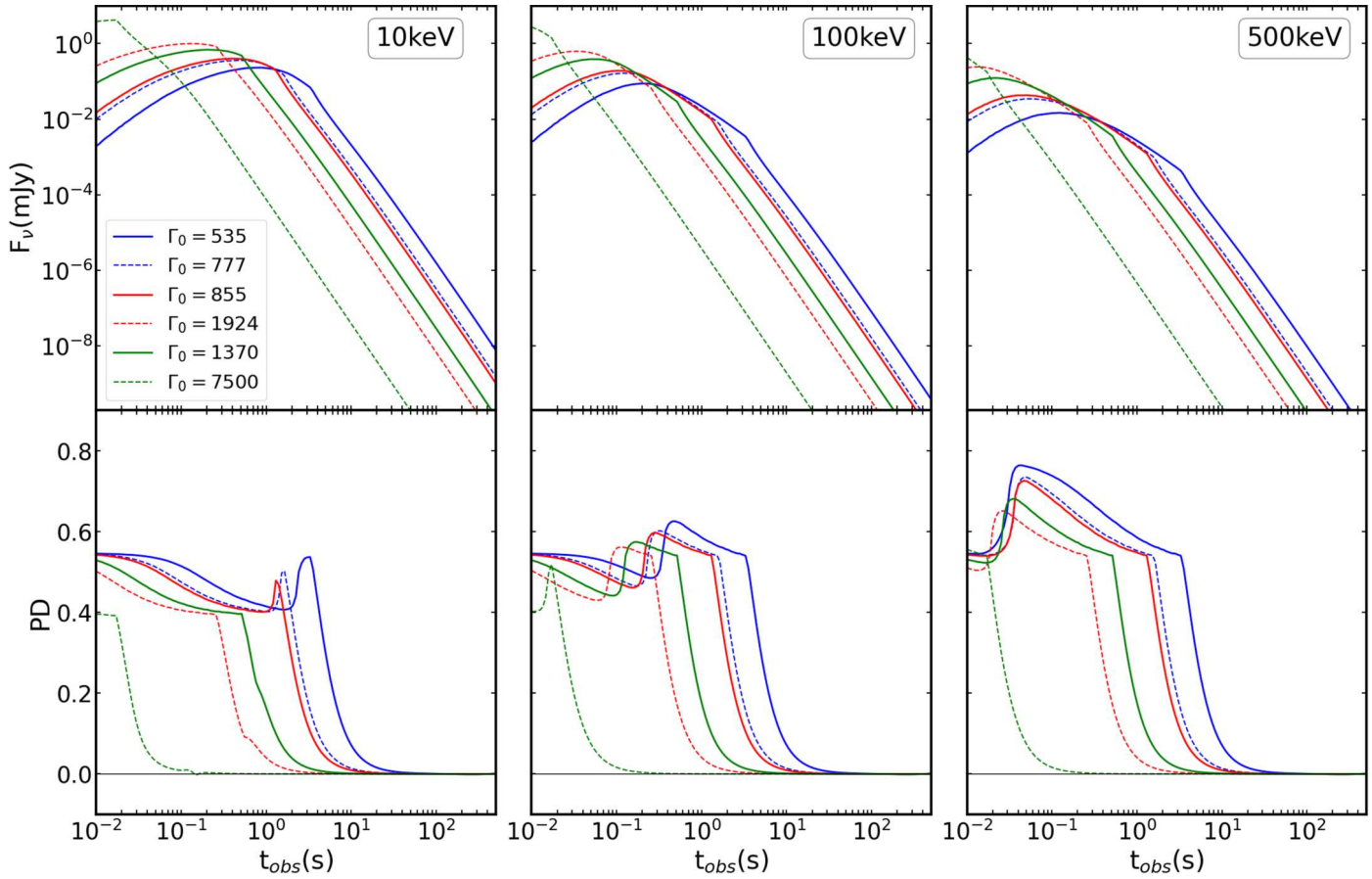

Figure 7. Light curves and polarization evolution of constant Γ models ($s = 0$). The blue, red, and green solid lines represent models sharing the same turn-off time as models [2a], [3a], and [4a], respectively. The blue, red, and green dashed lines represent models with the same bulk Lorentz factor as models [2a], [3a], and [4a] at the turn-off radius. respectively. The top panels show the light curves, while the bottom panels display the polarization degree curves. The left, middle, and right panels correspond to $h\nu = 10$, 100, and 500 keV, respectively.

constant Γ models (with $s = 0$) that feature higher bulk Lorentz factors. The new models with $\Gamma = 535$, 855, and 1370 have the same turn-off times as the [2a], [3a], and [4a] models, respectively. Additionally, the bulk Lorentz factors at the turn-off radius for models [2a], [3a], and [4a] are $\Gamma = 777$, 1924, and 7500, respectively. These models, characterized by $\Gamma = 777$, 1924, and 7500, are additional new models. All other parameters remain consistent with "a" models, and here we only calculate on-beam emission ($q = 0.6$). The results are shown in Figure 7.

The results of constant Γ models reveal that jets with lower Lorentz factors exhibit lower flux and polarization degree but do not alter the polarization decay slope significantly. Acceleration jets display higher initial polarization degrees compared to these constant Γ models, yet experience a faster polarization decline when they enter into high-latitude emission. Additionally, none of the constant Γ models exhibited a polarization angle flip.

In constant Γ jets, a flip in the polarization angle for on-beam emission requires the value of $\theta_j \times \Gamma$ to exceed a critical threshold (K. Cheng et al. 2024). In the model presented in this paper, with a viewing angle $q = 0.6$, a very large Lorentz factor Γ_0 would be necessary to observe polarization angle flips in a jet moving at a constant speed. Even with $\Gamma = 7500$, observing this phenomenon is challenging. However, polarization angle flips are more readily observable in acceleration jets. For instance, with $s = 1/3$, a noticeable flip occurs, which the bulk Lorentz factor ultimately reaches to only $\Gamma = 777$ when magnetic field strength decays. This significantly lowers the bulk Lorentz factor threshold required to observe the polarization angle flip.

While an accelerating jet initially resembles a constant bulk motion jet with a smaller bulk Lorentz factor—especially when only a small portion enters the field of view and the bulk Lorentz factor is uniformly distributed in the observed region—its behavior evolves over time. At later times, the acceleration jet is not simply dominated by large values of Γ; instead, emission from various radii contributes, resulting in a distribution of both bulk Lorentz factor and magnetic field strength with θ on an EATS. Closer to the LOS, the bulk Lorentz factor is larger and the magnetic field strength weaker.

To investigate the time when polarization angle first flips, we also calculated PD(θ) and $f_\nu(\theta)$ for purely acceleration models, magnetic dissipation models, and constant Γ models at $t_{\rm obs} = 100$ s, as shown in Figure 8. In acceleration models, with large acceleration index, the local flux no longer decreases monotonically with increasing θ. Instead, due to the diminished Doppler effect, faster-acceleration jets exhibit lower local flux at larger radius (closer to the LOS). Magnetic dissipation exacerbates this trend, suppressing the flux near the LOS. Conversely, for constant Γ jets (see Figure 8, right panels), jets with a smaller bulk Lorentz factor display a higher flux at later times, but all exhibit a similar decay trend. This explains why jets with acceleration and decaying magnetic field strength are more likely to exhibit polarization angle flips and higher polarization degrees after the flip.

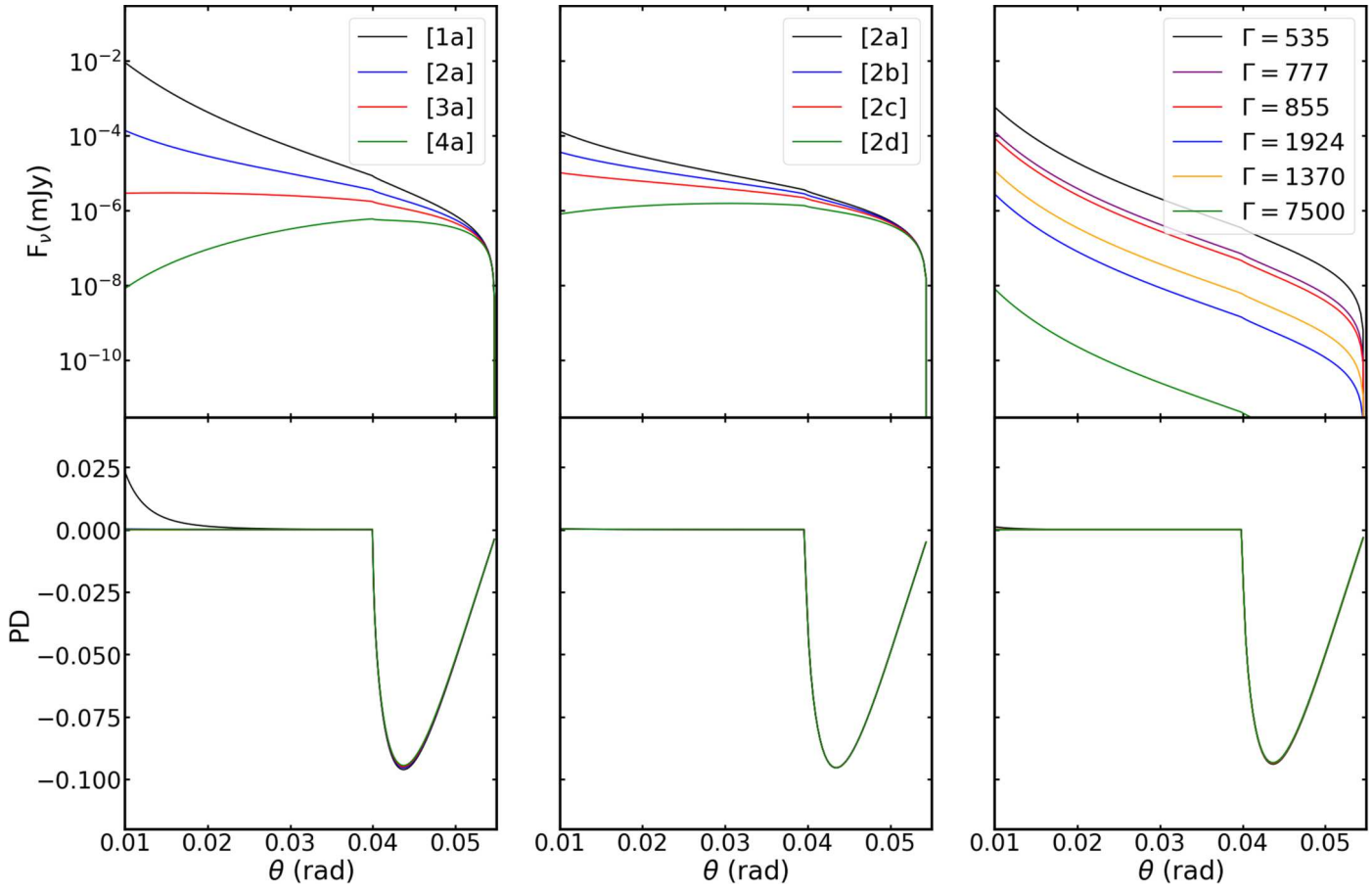

Figure 8. Distribution of local observed flux density and polarization with θ, 500 keV, $t = 100$ s. The top panels show the distribution of flux with θ, and the bottom shows the polarization of PD(θ) with θ. Purely accelerated models are shown in the left panels. Acceleration with magnetic dissipation models is shown in the middle panels, and constant Γ models are shown on the right side.

For the viewing angle of $q = 0.6$, the maximum local polarization degree following the polarization angle flip is approximately 10%, representing the theoretical upper limit of the observed polarization degree achievable under such conditions. This maximum is highly sensitive to the viewing angle. For off-beam emission at $q = 1.1$, the maximum polarization increases to approximately 20%, indicating that larger viewing angles result in a stronger polarization signal after the flip.

5. Conclusions

Poynting-flux-dominated jets undergo bulk acceleration during the prompt emission phase. In this paper, we use thin-shell models that expand radially, where the bulk Lorentz factor increases with radius. As bulk acceleration is linked to magnetic dissipation, the magnetic field strength may decrease with radius at the same time, i.e., $\Gamma = \Gamma_0(r/r_{\rm on})^s$ and $B = B_0(r/r_{\rm on})^{-(1+b\cdot s)}$. Our main results are given below.

1. Magnetic dissipation leads to a slower rise and decline in the light curve. For on-beam emission, a smoother decline in the polarization degree is observed before it drops to zero, whereas off-beam emission exhibits a steeper decline.
2. Faster acceleration and stronger magnetic dissipation facilitate easier polarization angle flips for small viewing angle observations and result in a higher post-flip polarization degree for large viewing angle observations.

During the early high-latitude emission, the dramatic decline of the light curve indicates that the jet undergoes bulk acceleration without significant magnetic dissipation (Z. L. Uhm & B. Zhang 2015). However, if the jet undergoes fast acceleration accompanied by magnetic dissipation, its light curve resembles that of a slower accelerating jet without magnetic dissipation, i.e., the light curve exhibits a smooth rise and decline before the turn-off time, followed by a shallower decay during the high-latitude emission phase. Due to the similar trends in the light curves of these two cases, it is essential to analyze the polarization evolution to distinguish them. For small viewing angles, a relatively smooth decline in the light curves, accompanied by polarization angle flips, indicates bulk acceleration and significant magnetic dissipation within the GRB jet. Otherwise, the jet is likely in the coasting phase. For large viewing angles, a gradual decline in the light curves, along with a high polarization degree after the flip, suggests bulk acceleration and magnetic dissipation. In contrast, the bulk Lorentz factor probably remains constant.

In addition, the similar origins of X-ray flares and prompt emission suggest that these findings are also applicable to the GRB X-ray flare. Notably, while the choice of the zero time affects the slopes of light curves, it has no impact on the polarization degree or the number of polarization angle flips. Therefore, polarization observations provide critical insights into the study of X-ray flares.

However, late-time polarization may currently be challenging to detect due to the low flux. Therefore, all the results require further validation through more sensitive polarization detectors in the future.

Acknowledgments

This work is supported by the National Key R&D Program of China (Grant Nos. 2024YFA1611700, 2021YFA071850X, 2021YFA071840X), the National Natural Science Foundation of China (grant Nos. 12027803, U1731239, 12133003, U1938201, 12273005) and the Guangxi Talent Program ("Highland of Innovation Talents").

ORCID iDs

Qian Zhong https://orcid.org/0009-0003-9058-1768
Hong-Bang Liu https://orcid.org/0000-0003-1695-3263
Kangfa Cheng https://orcid.org/0009-0004-3324-8421
Zu-Ke Feng https://orcid.org/0009-0001-4885-0747
Jiang-Chuan Tuo https://orcid.org/0009-0002-3780-892X
Jirong Mao https://orcid.org/0000-0002-7077-7195
En-Wei Liang https://orcid.org/0000-0002-7044-733X

References

Band, D., Matteson, J., Ford, L., et al. 1993, ApJ, 413, 281
Cheng, K., Zhao, X., Mao, J., & Chen, Z. 2024, A&A, 687, A128
Cheng, K. F., Zhao, X. H., & Bai, J. M. 2020, MNRAS, 498, 3492
Drenkhahn, G. 2002, A&A, 387, 714
Drenkhahn, G., & Spruit, H. C. 2002, A&A, 391, 1141
Feng, Z.-K., Liu, H.-B., Xie, F., et al. 2024, ApJ, 960, 87
Gao, H., & Zhang, B. 2015, ApJ, 801, 103
Geng, J.-J., Huang, Y.-F., Wu, X.-F., Song, L.-M., & Zong, H.-S. 2018, ApJ, 862, 115
Gill, R., & Granot, J. 2021, MNRAS, 504, 1939
Gill, R., Kole, M., & Granot, J. 2021, Galax, 9, 82
Granot, J., Komissarov, S. S., & Spitkovsky, A. 2011, MNRAS, 411, 1323
Kole, M. 2019, ICRC, 36, 572
Kole, M., De Angelis, N., Berlato, F., et al. 2020, A&A, 644, A124
Kumar, P., & Zhang, B. 2015, PhR, 561, 1
Lan, M.-X., & Dai, Z.-G. 2020, ApJ, 892, 141
Lan, M.-X., Wang, H.-B., Xu, S., Liu, S., & Wu, X.-F. 2021, ApJ, 909, 184
Lan, M.-X., Wu, X.-F., & Dai, Z.-G. 2016, ApJ, 816, 73
Lazar, A., Nakar, E., & Piran, T. 2009, ApJL, 695, L10
Lazarian, A., & Vishniac, E. T. 1999, ApJ, 517, 700
Li, J.-S., Lan, M.-X., & Wang, H.-B. 2024, ApJ, 970, 10
McKinney, J. C., & Uzdensky, D. A. 2012, MNRAS, 419, 573
Meszaros, P., & Rees, M. J. 1993, ApJ, 405, 278
Parker, E. N. 1957, JGR, 62, 509
Pearce, M., Eliasson, L., Kumar Iyer, N., et al. 2019, APh, 104, 54
Rees, M. J., & Meszaros, P. 1994, ApJL, 430, L93
Rossi, E. M., Lazzati, D., Salmonson, J. D., & Ghisellini, G. 2004, MNRAS, 354, 86
Ryan, G., Eerten, H. V., Piro, L., & Troja, E. 2020, ApJ, 896, 166
Rybicki, G. B., & Lightman, A. P. 1979, Radiative Processes in Astrophysics (New York: Wiley-Interscience)
Sari, R. 1998, ApJL, 494, L49
Sui, L.-Q., & Lan, M.-X. 2024, MNRAS, 529, 4287
Thompson, C. 1994, MNRAS, 270, 480
Toma, K., Sakamoto, T., Zhang, B., et al. 2009, ApJ, 698, 1042
Tuo, J.-C., Liu, H.-B., Mai, Q.-N., et al. 2024, ApJ, 973, 113
Uhm, Z. L., & Zhang, B. 2014, NatPh, 10, 351
Uhm, Z. L., & Zhang, B. 2015, ApJ, 808, 33
Uhm, Z. L., & Zhang, B. 2016a, ApJL, 824, L16
Uhm, Z. L., & Zhang, B. 2016b, ApJ, 825, 97
Uhm, Z. L., Zhang, B., & Racusin, J. 2018, ApJ, 869, 100
Vlahakis, N., & Königl, A. 2003, ApJ, 596, 1104
Wilson-Hodge, C. A., McConnell, M., Ajello, M., et al. 2021, BAAS, 53, 135.02
Wu, X. F., Dai, Z. G., Huang, Y. F., & Lu, T. 2005, MNRAS, 357, 1197
Zhang, B., & Yan, H. 2011, ApJ, 726, 90